IEEE Access
Multidisciplinary ⋮ Rapid Review ⋮ Open Access Journal

Received 30 July 2024, accepted 20 September 2024, date of publication 23 September 2024, date of current version 7 October 2024.

Digital Object Identifier 10.1109/ACCESS.2024.3466393

RESEARCH ARTICLE

The Interaction Between Electric Field and Partial Discharges Simultaneously Detected in a HVDC Cable Under Operating Conditions

ALESSIO DI FATTA[1], (Member, IEEE), PIETRO ROMANO[1], (Senior Member, IEEE), GIUSEPPE RIZZO[2], (Member, IEEE), GUIDO ALA[1], (Senior Member, IEEE), AND ANTONINO IMBURGIA[1], (Member, IEEE)

[1]L.E.PR.E. HV Laboratory, Department of Engineering, University of Palermo, 90133 Palermo, Italy
[2]Prysmian, 20126 Milan, Italy

Corresponding author: Antonino Imburgia (antonino.imburgia01@unipa.it)

This work was supported in part by European Union-Fundo Social Europeu (FSE), Programma Operativo Nazionale (PON) Research and Innovation 2014–2020 under Project DM 1062/2021; and in part by the Progetti di Rilevante Interesse Nazionale (PRIN) 2020-Innovative Solutions for Renewables in Energy Communities (ISoREC).

ABSTRACT The reliability assessment of HVDC systems greatly depends on the insulating materials aging level and, among these, the cable insulation layer plays a fundamental role. With this in mind, in this work, the correlation between the electric field distribution and the triggering and evolution of PD in a DC cable containing an internal air void defect and subjected to normal operating conditions has been investigated. The aim is to demonstrate that the PD activity under DC depends on the electric field distribution which, in turn, is related to the conductivity gradient that varies with load. In a previous paper, the field distribution in a cable specimen was simulated. Here, instead, the field profiles have been experimentally obtained starting from the measured space charges detected simultaneously with the PD activity. For the charge detection and for the PD monitoring, an innovative PEA cell and a PD acquisition system have been used, respectively. Measurement results highlight that the PD behavior depends on both the electric field distribution and the time constant τ. Specifically, during the first 10 minutes of the beginning of the test, the field in the outer cable radius passes from 12 to 17 kV/mm and it is maintained around this last value until 30 minutes. PD are triggered after 1 minutes from the start of the test, corresponding to a PDIEF of 12.6 kV/mm calculated in the healthy cable section. The detected PD activity shows a PDRR with maximum value equal to 110 pulse/min at the beginning of the test. Whereas, after 15 minutes, the electric field variation *dE/dt* is approximately zero and the PDRR, that is maintained only by τ, results around 10 pulse/minute.

INDEX TERMS Electric field, HVDC, partial discharge, PEA, space charge.

I. INTRODUCTION

In medium and high voltage electrical grids, the monitoring of their health status is essential to prevent failures. In the insulating layer of components employed in these systems (e.g. cables, joints and terminations) the main causes of lifetime reduction are attributed to electrical, thermal and mechanical stresses [1]. These can act alone or in combination between them as a cause of ageing phenomenon, but also they can promote other degradation factors as the onset of Partial Discharges (PD) phenomenon [2], [3]. The theoretical knowledge and the practical detection of PD are well consolidated under AC stress [4], [5]. On the contrary, for DC systems, further considerations and studies are needed to clarify the occurrence of PD activity [6], [7].

A significant difference between AC and DC power cables concerns the electric field distribution within the insulating layer. Under AC voltage waveform the electric field profile is always Laplacian with maximum and minimum values in correspondence of the inner-semicon/insulation and insulation/outer-semicon interfaces, respectively [8].

The associate editor coordinating the review of this manuscript and approving it for publication was Chandan Kumar.

© 2024 The Authors. This work is licensed under a Creative Commons Attribution-NonCommercial-NoDerivatives 4.0 License.
For more information, see https://creativecommons.org/licenses/by-nc-nd/4.0/

Under DC voltage stress, the field distribution is Laplacian only at the beginning and in case of zero load. While, under normal operating conditions, the occurrence of temperature gradient generates a conductivity gradient that, in turn, promotes the injection and accumulation of space charge in the insulation [9]. This phenomenon influences the radial electric field distribution profile that, in some cases, could shows the inversion of the initial Laplacian distribution with the maximum and minimum values in correspondence of the insulation/outer-semicon and inner-semicon/insulation interfaces, respectively [10], [11]. In the literature, several recent works focused on both simulations and measurements of electric field behavior under DC stress were proposed. Teyssedre et al. conducted a study on the effect of electric field distribution in insulating materials for HVDC cable joints under transient regime [12]. Whereas, in [13], the electric field inversion in DC cable insulation under thermal gradient was observed by means of two different simulation models. Further works based on simulations approach have been published by Ren et al. in [14]. In that work the analysis concerning the impact of the radial nonuniform conductivity under thermal gradient, that influences the accumulation of charge, on the electric field distribution of HVDC xlpe cable was investigate. It was found that the conductivity value decreases with the cable radius and strongly influences the field profile. In addition to that investigated in [14] and [15] the accumulation of space charge and its effect on the electric field profile during polarity reversal has also been simulated. In [16], the electric field has been simulated in a three layers specimen of xlpe with embedded an air void defect, whereas the PD has been experimentally detected. Results highlight the increasing of electric field gradient at high temperature that, in turn, leads to the triggering of PDs at lower supply voltage. Beyond the electric field simulation, the PD behaviour in four different defect types that can be present on HVDC cables has been measured in [17]. Final results show that the most serious electric field distortion is given by corona defect. In [18] the electric field and the PD occurrence for different cavity shapes embedded in a xlpe specimen have been simulated and provide as result that the elliptical void shape in respect to the spherical one, shows the highest PD magnitude. With regards experimental tests, in [19] the effect of cable aging on the PD inception voltage has been evaluated. In particular, it that paper it was found that for increasing aging the inception voltage is reduced due to the increment of dielectric conductivity that, in turn, promotes the space charge accumulation. While, Cavallini et al. in [20], subjected a specimen containing an air void defect to the DC stress. Before and after the DC polarization the PD activity under AC voltage has been investigated. The carried out evaluation shows that the space charge accumulation affect PD phenomenology.

In [21], it was suggested that for HVDC transmission networks operating under dynamic conditions, due to the continuous variation of the radial electric field, the design of the insulation system should be customized for each specific application based on a priori knowledge of the operating conditions.

This radial distribution variability of the electric field value over time strictly influences the PD inception conditions. However, for a fixed applied DC voltage level, infinite different electric field distributions, depending on multiple factors, can be associated. For this reason, under DC, results more appropriate considered the PD Inception Electric Field (PDIEF) rather than the PD Inception Voltage (PDIV) which is typically used in AC systems [21].

Based on the above, in a cable section containing an air void defect, for a fixed voltage stress, the triggering and the evolution of PD activity will be strictly dependent on the defect location along the dielectric radius.

In a previous paper published by the authors [22] the electric field inversion phenomenon, due to the accumulated space charge, has been indirectly observed by means of the triggering of PD. In particular, a DC model cable containing an air void defect located in the external dielectric/semicon interface was subjected to both DC stress and thermal gradient. Under 60 kV DC stress and from zero load to thermal regime the PD activity was experimentally monitored, while the electric field distribution was simulated by means of Comsol Multiphysics software. Results showed that at the time in which the PD were triggered, the simulated electric field along the cable radius was reversed and reached a value equal to 18 kV/mm within the air void. Therefore, the effect on the electric field inversion on the PD activity was indirectly demonstrated by observing the PD onset.

On the basis of the above, the innovative development proposed in the present article, in respect to [22], concerns the experimentally detection of the electric field distribution simultaneously with the monitoring of PD activity. This with the aim to observe the effect of the electric field profile changes on the occurrence of PD. A difference between the previous and present experimental tests consist in the fact that in [22] PD measurements were carried out under thermal and electrical transient, while in this work the acquisitions begin after reaching the thermal steady state. The electric field, in each instant of time, is calculated starting from the measured space charge in a healthy cable section. While, the PD have been monitored by means of a commercial PD monitoring instrument with the sensor placed in contact with the cable and in correspondence of the air void defect. From the obtained Time Resolved PD (TRPD) pattern, the identification of internal PD signals has been carried out by using a cross-correlation-based clustering algorithm which is able to separate pulses according to their similarity [23].

As regards the detection of space charge profiles, the Pulsed Electro-Acoustic (PEA) technique has been adopted [24]. To obtain clear charge distributions, a new PEA cell has been built on the basis of the innovative configuration proposed by Zahara et al. in [25]. Its working principle and the comparison with the traditional PEA cell structure are

reported in the next Section II. Whereas, the signal processing that leads from the acquired PEA signals to the electric field distributions, is theoretically described in Section III. After that, the arranged experimental setup and the adopted measurement procedure are illustrated in Section IV. Finally, in Section V, the obtained measurement results concerning the space charge and the related electric field distributions, as well as the detected PD pulses and its clustered pattern, are reported and discussed.

However, the research gap provided with the present work mainly concern the experimentally simultaneous detection of space charge and PD phenomena in a model cable subjected normal operating conditions. The proposed measurement setup and the detailed description of the new PEA cell and the space charge signal process to calculate the electric field as well as the PD signal clustering process to obtain the final understandable PD patters, provide useful instructions and information to readers for repeating and improving this research activity. Finally, the following illustrated simultaneous detection, which has been carried for the first time in this work, allows to clarify the correlation between the two main HVDC dielectric degradation factors, such as space charge and PD.

II. WORKING PRINCIPLE OF THE PEA METHOD AND COMPARISON BETWEEN THE TRADITIONAL AND THE NEW BUILT PEA CELL STRUCTURE

The main used technique for the detection of space charge in solid dielectrics is the PEA method [24]. Considering that for cable specimens the traditional PEA cell provides an output signal that is affected by a high attenuation factor, a new version of the PEA cell has been built. In the following, for better understanding the advantages provided by the new structure, an in deep comparison analysis of both traditional and new technologies is carried out.

The general working principle of the PEA technique is mainly based on the generation, propagation and detection of acoustic waves. To promote the charge formation and accumulation in the cable dielectric layer a high voltage DC generator is needed. While, a pulse generator is used to vibrate the accumulated charges. This last generator is applied by means of two metal electrodes wrapped around the cable and in correspondence of the measuring point (such as the point in which the PEA cell is placed). From the charge vibration, acoustic waves are generated and then detected from a piezoelectric sensor inserted in contact with the ground electrode of the PEA cell. The piezoelectric sensor converts the acoustic pressure waves into voltage electrical signals which are then sent, after amplification, to the oscilloscope and computer for their visualization and elaboration [24]. The signal processing, for the conversion from the electrical to a charge signal will be explained in the next Section.

In Fig. 1, the block schemes of the traditional and the new PEA cell structures are reported. In general, for cable specimens stressed with positive voltage, positive and negative charges accumulate in correspondence of the inner semicon/dielectric and dielectric/outer semicon interfaces, respectively [26]. Depending on the duration and magnitude level of the voltage application and on the thermal gradient, a different amount of space charge accumulates in both interfaces as well as in the dielectric bulk [27]. However, for a simply explanation and description of the acoustic waves behavior within the PEA cells, in the present study only the single positive interfacial charge is considered.

As is well known, when an acoustic wave reaches an interface between two different materials it is partially transmitted and partially reflected in the opposite direction. For both PEA cell structures, the transmitted acoustic waves are reported in red color, while the reflected waves in each interface are highlighted in blue color. The thickness of each depicted wave gives a rough indication of the acoustic wave amplitude, while the exact values can be obtained starting from the transmission K^T and the reflection K^R coefficients, which are given by equations (1). These coefficients are computed in each PEA cell component interface and are dependent from the acoustic impedances Z (which is given by the product between sound velocity v and volumetric density ρ of each material) of the two materials in contact to each other [28].

$$K^{T}_{i-j} = \frac{2Z_j}{Z_i + Z_j} \quad K^{R}_{i-j} = \frac{Z_j - Z_i}{Z_i + Z_j} \tag{1}$$

In equations (1), the subscript i indicates the material from which the wave is generated or come from, while the subscript j indicates the material from which the wave is traveling.

In Table 1, the calculated Z values of the materials involved in both PEA cell structures are reported.

For a better comparison between the acoustic wave behaviour within the two PEA cell structures, the calculated values of K^T and K^R coefficients, in addition to being illustrated in Fig. 1, are also reported in Table 2. For both structures, the effect of the outer semicon layer on the acoustic waves' behavior is neglected due to the similar value of the acoustic parameters between this material and the dielectric.

Concerning the traditional PEA cell structure, with block scheme depicted in Fig. 1a, the acoustic wave generated from the vibrated positive charge travels through the cable dielectric layer, then passes through the ground electrode made of aluminum material and after it reaches the piezoelectric sensor. In contact with the last component, with the task of absorbing the acoustic wave and thus to avoid multiple wave reflections, an absorber layer made of the same material of the piezoelectric sensor, such as PolyVinyliDene Fluoride (PVDF), is employed.

As can be observed in Fig. 1a, when the acoustic wave, traveling from the inner semicon/dielectric interface, or, in general, from a charge deposited within the dielectric bulk, reaches the dielectric/outer semicon interface, it is partially

transmitted (red wave) in the sensor direction and partially reflected (blue wave) in the opposite direction.

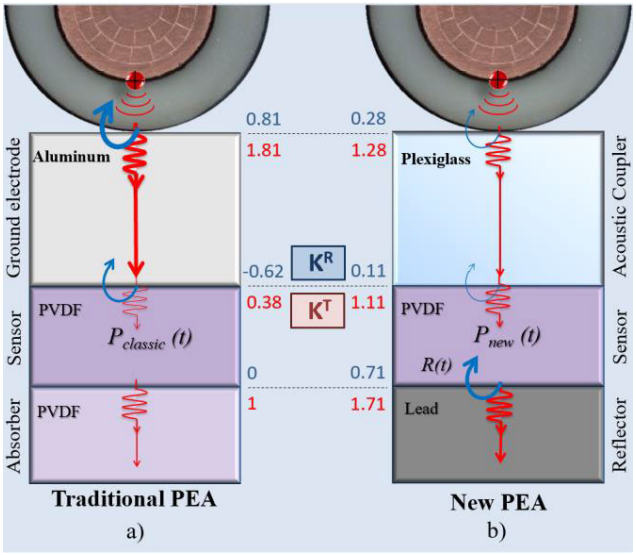

FIGURE 1. Acoustic wave behavior within the a) traditional and b) the new PEA cell structures. The calculated transmission K^T and the reflection K^R coefficients are reported for each interface in red and blue color, respectively. The thicknesses of the direct (red) and reflected (blue) waves approximately indicate their signal amplitude.

TABLE 1. Acoustic impedances of each material involved in the acoustic wave path for both traditional and new PEA cell structures.

Material	v [m/s]	ρ [kg/m3]	Z [Ns/m^3]
Xlpe	2200	920	$1.8{\cdot}10^6$
Aluminum	6420	2690	$17.3{\cdot}10^6$
Plexiglass	2720	1190	$3.2{\cdot}10^6$
PVDF	2260	1780	$4{\cdot}10^6$
Lead	2160	11300	$24.2{\cdot}10^6$

TABLE 2. Transmission and reflection coefficients of each materials interfaces for both traditional and new PEA cell structures.

PEA cell version	Interface	K^T	K^R
Traditional	Xlpe/Aluminum	1.81	0.81
	Aluminum/PVDF	0.38	-0.62
	PVDF/PVDF	1	0
New	Xlpe/Plexiglass	1.28	0.28
	Plexiglass/PVDF	1.11	0.11
	PVDF/Lead	1.71	0.71

In particular, for the xlpe DC cable under test, in correspondence of the xlpe/ground-electrode interface, due to the Z values of the two materials, K^T and K^R are equal to 1.81 and 0.81, respectively. Therefore, the transmitted acoustic wave is amplified and equal to the 181% of the incident wave. Whereas the reflected part of the wave is equal to the 81% of the incident one. However, this positive wave amplification effect of 181% falls away in correspondence of the ground-electrode/sensor interface. This because in this last interface, where $K^T = 0.38$ and $K^R = -0.62$, only the 38% of the incident wave propagating through the ground electrode is sensed by the piezoelectric sensor. Finally, in the sensor/absorber interface, because these components are made with the same material, the transmission and the reflection coefficients are equal to 1 and 0, respectively. This means that the wave passing through the sensor is totally transmitted in the absorber direction to be absorbed.

In conclusion, neglecting the acoustic wave attenuation along its path, the total pressure wave detected by the piezoelectric sensor is equal to the 37.56% of the 181% and thus its results 68% of the generated acoustic wave.

As can be deduced from Fig. 1a, the acoustic wave generated in the inner semicon/xlpe interface, before crossing the ground electrode, has to pass through the entire dielectric layer. For this reason, the signal related to this interfacial charge is subjected to a higher wave attenuation phenomenon due to the high acoustic wave attenuation factor of the dielectric material. For this reason, one of the main PEA technique limitations, especially for application on full-size cables, is that the obtained charge output signal related to inner semicon/dielectric interface results very low in magnitude and sometimes overlapped by signals noise and reflections [26], [27], [28], [29], [30], [31].

A solution to this problem has been found by Zahara et al. [25], in which some materials of the traditional PEA cell structure were changed. In particular, the aluminum and the PVDF materials of the ground electrode and the absorber components have been replaced by PMMA (commonly known as plexiglass) and brass, respectively.

The PMMA (with Z value closer to that of the PVDF material) block, now called "Acoustic Coupler", allows a better acoustic match between it and the piezoelectric sensor. Whereas, compared to the structure proposed in [23], for reasons linked to the availability, cost and workability of material, in our PEA cell structure a piece of lead has been used instead of brass as absorber component.

The new PEA cell structure is schematically reported in Fig. 1b. In this configuration the K^T coefficients in the dielectric/acoustic-coupler interface and in the acoustic-coupler/sensor interface are equal to 1.28 and 1.11, respectively. This means that the generated positive acoustic wave is firstly amplified by 128% when pass through the plexiglass, and then it is amplified again by 111.11% when reaches the sensor. Therefore, the direct acoustic wave sensed by the sensor is equal to the 142.22% of the wave generated in the inner semicon/dielectric interface. Moreover, thanks to the lead used as absorber, which is now called "Reflector", the acoustic wave passing through the sensor is not absorbed as in the traditional PEA cell, but it is partially reflected, with $K^R = 0.7161$, in the sensor/reflector interface. This means that, the 142.22% of the direct detected wave that passed though the sensor, when reaches the lead is for the 71.61% reflected in the sensor direction. The 71.61% of the 142.22% results 101.84%. This reflected wave is added to the direct wave and thus the total acoustic wave sensed by the sensor

is given by their sum that results equal to the 244% of the generated wave.

The ratio between the total pressure waves detected by the piezoelectric sensor in the new (244%) and in the traditional (68%) PEA cell provides the increasing of acoustic wave sensitivity by a factor of 3.58 with the new PEA cell.

To confirm what was found, it is possible to evaluate the total pressure wave detected by the piezoelectric sensor in the traditional PEA cell as the product between the involved transmission coefficients [25], [30]:

$$P_{\text{Traditional}} = K^{T}_{\text{xlpe}-\text{Al}} \cdot K^{T}_{\text{Al}-\text{PVDF}} = \frac{2Z_{\text{Al}}}{Z_{\text{Al}} + Z_{\text{xlpe}}} \cdot \frac{2Z_{\text{PVDF}}}{Z_{\text{PVDF}} + Z_{\text{Al}}} = 0.68 \quad (2)$$

whereas, in the new PEA cell structure, the contribution provided by the reflection coefficient in the PVDF/lead interface must also be considered [25]. Therefore, a second term related to the entire path taken by the reflected wave is inserted in the expression (3).

$$\begin{aligned} P_{\text{New}} &= \left[K^{T}_{\text{xlpe}-\text{plex}} \cdot K^{T}_{\text{plex}-\text{PVDF}}\right] \cdot \left[K^{T}_{\text{xlpe}-\text{plex}} \cdot K^{T}_{\text{plex}-\text{PVDF}} \cdot K^{R}_{\text{lead}-\text{PVDF}}\right] \\ &= \left[\frac{2Z_{\text{plex}}}{Z_{\text{plex}} + Z_{\text{xlpe}}} \cdot \frac{2Z_{\text{PVDF}}}{Z_{\text{PVDF}} + Z_{\text{plex}}}\right] \cdot \left[\frac{2Z_{\text{plex}}}{Z_{\text{plex}} + Z_{\text{xlpe}}} \cdot \frac{2Z_{\text{PVDF}}}{Z_{\text{PVDF}} + Z_{\text{plex}}} \cdot \frac{Z_{\text{lead}} - Z_{\text{PVDF}}}{Z_{\text{PVDF}} + Z_{\text{lead}}}\right] \\ &= 2.44 \end{aligned} \quad (3)$$

The increment of sensitivity with the new PEA cell, as in the previous case, is given by the following ratio:

$$\frac{P_{\text{new}}}{P_{\text{Traditional}}} = \frac{2.44}{0.68} = 3.58 \quad (4)$$

In Fig. 2 the photograph of the built new PEA cell sensor is reported.

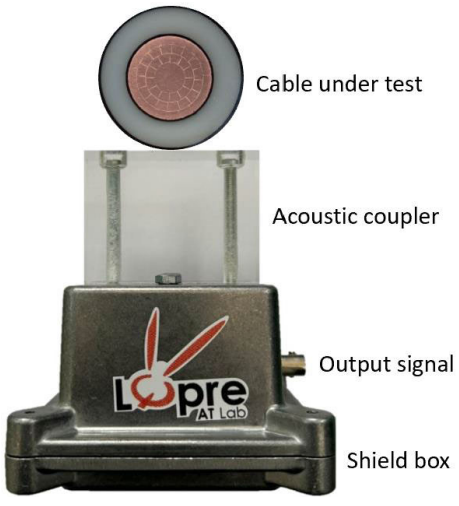

FIGURE 2. The new PEA cell sensor.

III. PEA SIGNAL PROCESSING

To gain information on the space charge distribution within the dielectric cable layer, the signal obtained from the PEA sensor at the output of the amplifier must be appropriately processed [32]. Fig. 3 shows the PEA profile acquired and chosen as base reference signal for the signal processing procedure. This is a time-varying voltage signal that must be converted into a volumetric charge density as a function of the cable radius. In addition, several processes must be implemented to correct the changes that the signal undergoes during the acquisition phase and which, if not considered, would lead to an incorrect interpretation of the results. The processing phase can generally be divided into six steps, where the last one concerns the transition from the charge profile to the electric field distribution.

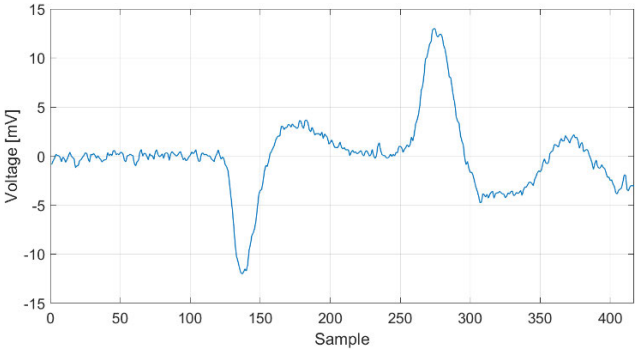

FIGURE 3. Space charge signal received from the new PEA cell.

A summary of the entire procedure is shown in the flow chart of Fig. 4, while each step is explained in the following subsections.

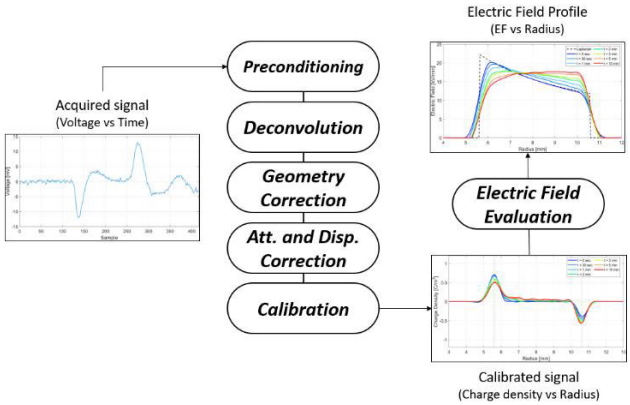

FIGURE 4. From PEA signal to electric field evaluation process.

A. STEP 1: PRECONDITIONING

Sometimes the acquired signal has characteristics that make it unsuitable for the deconvolution process. Due to factors dependent on the measurement setup, the profile has an offset that can be corrected either during the measurement

itself, through the oscilloscope settings, or during the post-processing phase through subtraction of the mean value. In addition, if a good coupling between the thickness of the piezo-electric sensor and the voltage pulse width is not realised, the PEA signal is positioned right at the tail of the latter. The result is a profile with an increasing (or decreasing) trend and thus a distorted baseline. Another software correction is then necessary to obtain a horizontal baseline. In this case, it was decided to subtract the signal acquired in the absence of applied DC voltage from the profile. At last, through the oscilloscope settings, it is possible to reduce the Signal-to-Noise Ratio (SRN) by evaluating the average profile among several successive acquisitions. The number of profiles to average can vary depending on the degree of noise during the measurement (from a few thousand to tens of thousands) [33].

B. STEP 2: DECONVOLUTION

Deconvolution is aimed to recovering the original signal after its convolution with the transfer function of the system consisting of the PEA cell [32]. Information about the transfer function must be extracted from the PEA profile's first peak, as the only deformation it undergoes is due to the cell. For this reason, deconvolution is applied between the acquired signal and the first peak only. Several techniques have been proposed in the literature for the application of the deconvolution procedure, and in general these can be distinguished into two categories: deconvolution in the time domain and deconvolution in the frequency domain [34], [35]. For this work, the Laplace deconvolution proposed by Yeongguk et al. in [36] has been used. This technique has been implemented in the MATLAB environment and works in the frequency domain. By using decreasing exponential functions as the weight applied to the two input signals, it is possible to obtain the Laplace transform through the application of the fast Fourier transform algorithm. This avoids having to work in symbolic form. The reason for choosing a frequency domain approach over a time domain approach is that the operations between the acquired signal and the transfer function are less computationally onerous.

C. STEP 3: GEOMETRY CORRECTION

For PEA measurements on cables (model or full-size), distortions introduced by the geometrical configuration must also be considered and corrected. The main differences with respect to the case of flat specimens are the different stress experienced by the charge due to the radial distribution of the electric field and the attenuation of the amplitude of the acoustic wave due to the distribution of energy over a surface of increasing radius during propagation. It is then necessary to proceed with a normalisation of the profile to make it equivalent to one obtained with a uniform field, as in the case of flat specimens, and to amplify the internal acoustic wave to compensate for the attenuation suffered. Both corrections are made through correction coefficients that are a function of the ratio between the outer radius and the various radial sections of the dielectric [32].

D. STEP 4: ATTENUATION AND DISPERSION CORRECTION

A further attenuation phenomenon is due to the dispersive and dissipative nature of the dielectric material. Only the peak generated at the internal dielectric interface undergoes this attenuation process due to propagation through the dielectric. To correct this phenomenon, the transfer function of the medium must be derived by comparing the acoustic wave at the inner and outer radius [25]. Specifically, attenuation and dispersion factors are to be derived. Then by the least squares method is applied to estimate the signal before attenuation based on the signal obtained after deconvolution [25].

E. STEP 5: CALIBRATION

All the previous steps are based on recovering the original signal, which in any case remains a voltage signal. The last step then is to convert the corrected measured signal into the space charge distribution expressed in C/m^3. In this case, the conversion is performed by evaluate the ratio between the integral of the first peak only and the expected surface charge density, based on the cable size and applied voltage. This gives the conversion coefficient to be applied to the entire signal [37].

F. STEP 6: FROM SPACE CHARGE TO ELECTRIC FIELD

Having determined the radial charge distribution, we proceed to calculate the electric field by applying the differential form of the Gauss law:

$$divE = \frac{\rho}{\varepsilon_0 \varepsilon_r} \tag{5}$$

where E is the electric field, ρ the volumetric charge density, ε_0 and ε_r are the permittivity of the vacuum and relative permittivity of the insulating medium.

Assuming that the charge depends only on the radius r, the following differential equation is obtained:

$$\frac{dE}{dr} + \frac{1}{r}E = \frac{\rho(r)}{\varepsilon_0 \varepsilon_r} \tag{6}$$

The general solution of (6) is given by:

$$E(r) = \frac{1}{r\varepsilon_0 \varepsilon_r} \int_{r_i}^{r} r\rho(r)\, dr + \frac{C}{r} \tag{7}$$

where r_i is the dielectric inner radius and C is a constant. The latter is chosen appropriately to enforce the condition that the integral of the field along the radius corresponds with the applied voltage U_{DC}:

$$\int_{r_i}^{r_o} E(r)\, dr = U_{DC} \tag{8}$$

where r_o is the dielectric outer radius.

IV. EXPERIMENTAL SETUP AND MEASUREMENT PROCEDURE

To simultaneously measure the accumulation of space charge, from which the electric field distributions are obtained, and the PD activity in a model cable subjected to both DC stress and thermal gradient, the arranged measurement setup is reported in Fig. 5.

It is mainly composed by a high voltage DC generator (Glassman High Voltage Series WR with maximum output voltage magnitude 125 kV), the xlpe model cable specimen, a pulse generator, a current transformer, the new PEA cell and the PD measuring system (Pry-Cam Grids monitoring system with Pry-Cam wings sensor). The cable under test, which contains an artificially made internal air void defect, is constituted of XLPE insulating material with thickness of 5mm. As regards the air void defect, it has been made with four steps. First of all, a rectangular portion of external semiconductor layer with dimension of two square centimetres has been accurately removed. Then, using a cutter, a hole with a depth of 1 mm and a diameter of 2 mm was created in the dielectric layer surface. As third step, to avoid unwanted air bubbles, silicone grease has been spread on the surface of the exposed dielectric, avoiding to occlude the defect. Finally, a new semiconducting layer, identical to the one removed, is repositioned in the cable and held in place with insulating tape.

The DC generator is used to apply the electrical stress and therefore to create the electric field within the cable dielectric layer. To faithfully reproduce the normal operating conditions, a thermal gradient in the cable section has been also created imposing a current flow by means of the current transformer. In these stress conditions the space charge accumulation phenomenon is promoted and it is measured by means of the PEA technique. Whereas, the PD acquisition instrument is used to detect the PD signals which occur for certain electrical and thermal stress conditions.

In the measurement setup a PT100 temperature sensor and a Rogowski current sensor, are also present. The first one is used to monitor the temperature of the external cable layer. The second sensor, instead, is used to monitor the current flowing through the model cable core. Starting from the measured current, the temperature inside the conductor, and thus in the core/dielectric interface, is calculated by means of a thermal model of the experimental setup implemented in a Finite Element Method (FEM) software.

By knowing both internal and external temperatures of the model cable, the thermal gradient is easily calculated along the cable length and it is in real time monitored for the entire test duration.

Considering that the air acts as a barrier for the acoustic wave propagation, the accumulation of charge cannot be directly measured within the air void defect [24]. For this reason, the PEA cell sensor has been placed in a different position in respect to the PD sensor. Therefore, the obtained electric field profiles, derived from the acquired space charges, are those related to the healthy cable section. In these conditions, the measurement is not affected by the charge distribution within the cavity. Field considerations within the cavity were made by simulation and comparison with the field obtained in the healthy dielectric section.

FIGURE 5. The arranged measurement setup for the simultaneous detection of space charge and PD in a DC model cable under operating conditions.

With regards the adopted measurement procedure, initially the thermal pre-conditioning of the cable, consisted in circulating a load current of 260 A within the cable core, has been made. At the thermal steady state, reached after 60 minutes, the calculated internal temperature results 46.5 °C, while the temperature of the external semiconductor layer, is equal to 35.5 °C. Therefore, at stationary regime the obtained thermal gradient within the dielectric layer results 11 °C. In Fig. 6, the calculated cable core temperature and that measured in the external cable layer, are depicted in black and red color, respectively.

As soon as the thermal steady state is reached, the HVDC and pulses generators are switched on and the simultaneous detection of space charge and PD starts (time t = 0 minutes). The applied DC stress has been chosen equal to 80 kV in positive polarity. Whereas, based on the cable thickness, to obtain a clear PEA cell output signal, the magnitude of the pulse generator, providing pulses with width 40 ns at trigger frequency of 110 Hz, has been fixed to 6 kV.

The duration of the entire test, without considering the thermal pre-conditioning phase, has been fixed to 40 minutes. From the beginning of the test to 30 minutes, both electrical and thermal stress have been applied, while, for 30 to 40 minutes the current flow has been reduced to zero. This in order to evaluate the electric field and PD behavior for decreasing

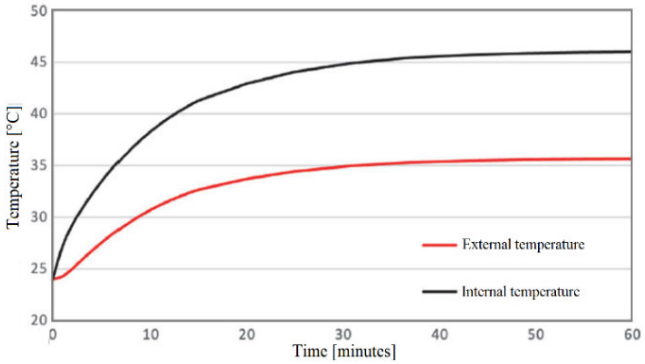

FIGURE 6. Thermal pre-conditioning of the cable under test. Temperature trend over time calculated the conductor (black) and measured at the outer surface of the cable (red).

thermal gradient values. The obtained measurement results are reported and discussed in the following Section.

V. ELECTRIC FIELD EVALUATION

With the switch on of the HVDC generator, the acquisition of space charge profiles has been started. The oscilloscope has been set to acquire a profile every 5 seconds. The first profile, characterised by the presence of only the surface charge due to the applied voltage, has been used as a reference for the determination of the correction factors and for the calibration process. Fig. 7 shows the charge profiles processed during the first 10 minutes, while Fig. 8 shows the corresponding electric field profiles. The initial electric field distribution (for t = 0 s) is superimposed on the theoretical Laplacian distribution. Differences near the inner and outer radius are due to the resolution of the PEA cell. The reversal process of the electric field is quite rapid and begins a few tens of seconds after the start of the test. 5 minutes after, the field in the outer region is greater than the field in the inner region. Fig. 9 and Fig. 10 show the charge and field profiles at 0, 10, 20 and 30 minutes, until the moment when the current flow in the cable is interrupted.

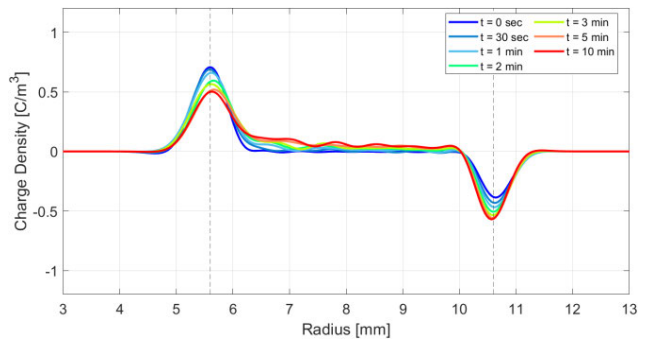

FIGURE 7. Detected space charge distribution during the first 10 minutes.

From 10 to 30 minutes there are no major changes in the field profile and therefore the inversion process can be described as stabilised. The small variations are due to fluctuations in the PEA signal due to background noise,

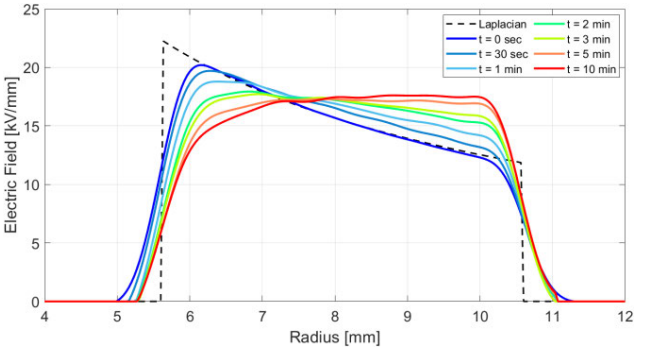

FIGURE 8. Related electric field profiles during the first 10 minutes.

which is not completely suppressed during the processing. In order to monitor the development of the electric field in the dielectric outer region in more detail, the maximum field in an interval of 0.5 mm near the outer radius has been evaluated for each acquired profile. The time distribution is shown in Fig. 11. The field outside has an initial value of 12 kV/mm. It increases rapidly to 16.5 kV/mm in the first five minutes, then settles at around 17 kV/mm after 10 minutes. Fig. 12 shows the trend of the simulated electric field inside the cavity. A trend practically identical to that calculated in a dielectric section without a cavity can be seen. In fact, in both cases the field increases in the first 10 minutes reaching a steady-state value. An offset of 5 kV/mm can be seen between the two trends in Fig. 11 and Fig. 12, due to the different dielectric permittivity inside the cavity and in the healthy dielectric section. An evaluation of the field profiles was not carried out after switching off the current flow. In fact, under these conditions, a dynamic phase begins in which the thermal gradient between the inside and outside of the cable undergoes a change. The different thermal conditions cause a change in the acoustic properties of the insulating medium and consequently in the transmission characteristics of the pressure wave. The calibration and correction procedure are calibrated for a specific thermal condition.

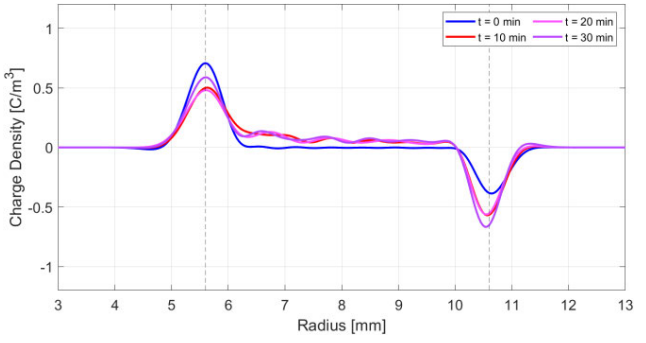

FIGURE 9. Detected space charge distribution during 30 minutes.

VI. PARTIAL DISCHARGE MEASUREMENTS

At the same time as the PEA measurement, the acquisition of PD has been started. Once a trigger threshold is set

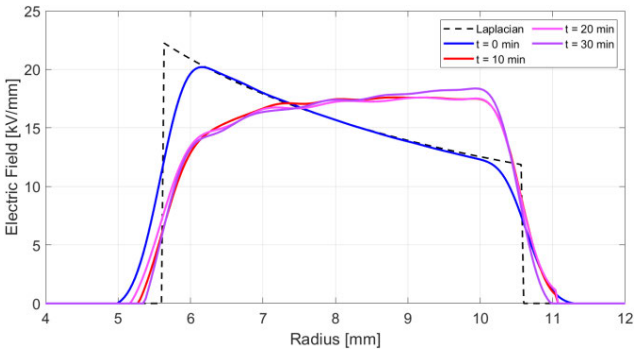

FIGURE 10. Related electric field profiles during 30 minutes.

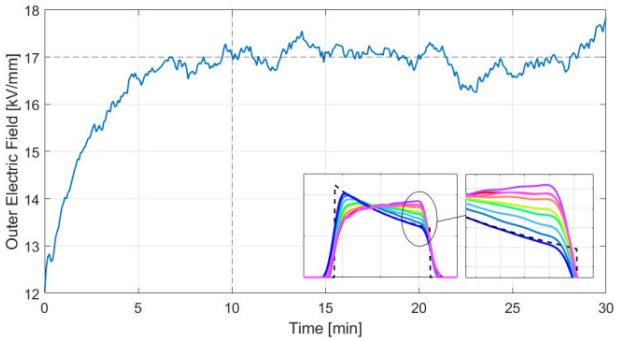

FIGURE 11. Maximum electric field values detected in the external cable insulating layer from 0 to 30 minutes.

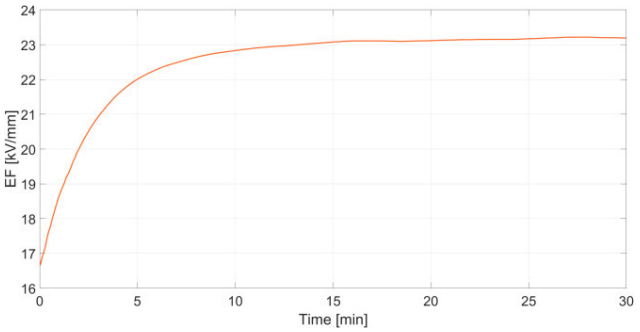

FIGURE 12. Simulated electric field values inside the cavity from 0 to 30 minutes.

(25.3 mV), the PD monitoring system detects and stores all pulses exceeding this threshold. To identify the nature of the discharges, the Phase-Resolved-Partial-Discharge (PRPD) Pattern is generally used in which signal amplitudes are mapped as a function of the phase angle of the AC supply voltage [38]. Clearly this type of map, which is useful for AC measurements, is ineffective for HVDC applications. Indeed, it is not possible to identify a waveform with which the discharge phenomena synchronise.

Fig. 13 shows the time distribution of the amplitudes, known as Time-Resolved-Partial-Discharge (TRPD) Pattern, while in Fig. 14 the related Time Frequency (TF) map is reported.

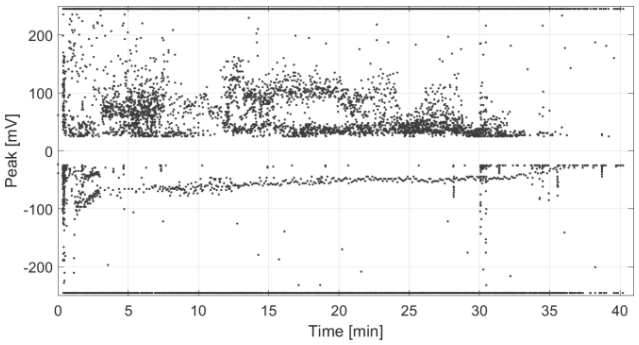

FIGURE 13. The obtained TRPD pattern during the entire test.

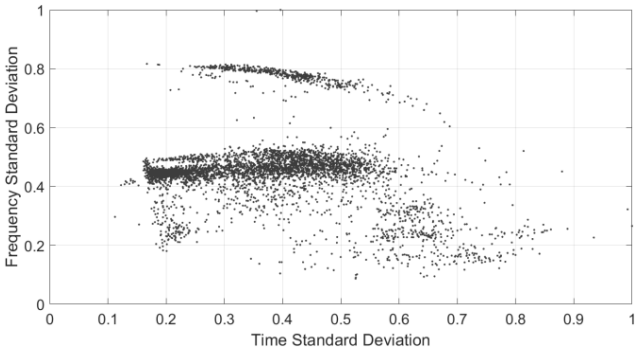

FIGURE 14. The related TF Map of the acquired PD dataset.

The quantities used to construct the TF map are derived from an analysis of the discharge signals s(t) performed in the time and frequency domain. In both cases, the signal is normalised with respect to its specific energy:

$$\tilde{s}(t) = \frac{s(t)}{||s||} = \frac{s(t)}{\sqrt{\int_0^T s(t)^2 dt}} \tag{9}$$

where $\tilde{s}(t)$ is the normalized signal and T the time duration of the signal. This results in a signal that, if squared, returns a non-negative function with an area equal to 1. These characteristics are typical of probability density functions, and consequently the statistic index used in the analysis of distributions can be used to summarise information on the temporal shape of the signal in a parameter σ_T evaluated with the same expression of the standard deviation:

$$\sigma_T^2 = \int_0^T (t - t_0)\, \tilde{s}(t)^2 dt \tag{10}$$

where t_0 is the expected value index. The same reasoning can be carried out on the frequency spectrum of the normalised signal, thus obtaining the σ_F parameter:

$$\sigma_F^2 = \int_0^{BW} (f - f_0) \left|\tilde{S}(f)\right|^2 df \tag{11}$$

where $\left|\tilde{S}(f)\right|$ is the module of the normalized spectrum, BW the frequency bandwidth and f_0 the frequency expected value index.

As can be seen in Fig. 13, a greater concentration in amplitude is observed for the negative pulses, while the positive ones are more diffuse. A vertical band of discharge can be seen in the initial phase, due to the increase in voltage during the power supply, and another band at the 30th minute. The heating transformer system has been switched off at this time. Despite these minor considerations, it is not possible to obtain further information on the nature of the acquired discharges, especially in the case where more than one phenomenon is detected. In the latter case, it is necessary to separate the different phenomena so that they can be analysed in more detail and without committing errors.

To isolate the discharges within the cavity from the rest of the acquired pulses, a clustering algorithm based on the signals waveform analysis by means of cross-correlation has been used [23], [39]. In brief, the algorithm associates a numerical value with the degree of similarity between the waveforms of two pulses to determine whether they belong to the same family of discharge. The evaluation of this parameter, called correlation coefficient, K_{cc}, is carried out by solving the following integral:

$$K_{cc} = \max \left| \int_{-\infty}^{\infty} x_1(t) \cdot x_2(t+\tau) \cdot dt \right| \tag{12}$$

where $x_1(t)$ and $x_2(t)$ are two generic signals. The range of values assumed by the coefficient goes from 0 to 1, where 0 indicates no correlation and 1 extreme similarity. Signals separation is performed by following the order in which the pulses are acquired and constructing a matrix in which each row represents a cluster. The first pulse is automatically included in the first row. To determine the family to which the n-th pulse acquired belongs, the correlation coefficient between it and the pulses belonging to the various clusters is evaluated. The choice falls on the cluster for which the highest K_{cc} value is obtained, if this meets a minimum value set by the user. If the condition on the minimum value is not met, the signal is considered not to belong to any family and a new cluster is generated. The main advantage of using this approach to clustering is that the separation of phenomena with different nature is based on the main index of this diversity, that is the shape of the pulse. The procedure is independent of the type of map used for the graphical representation of the data, unlike traditional clustering techniques such as DBSCAN or hierarchical clustering [40]. As a result, the algorithm can separate phenomena with overlapping patterns, which are difficult to detect with position-based clustering methods. Data division into clusters is visualized in the map by simply changing the colour of the discharges that fall into the same group. Consequently, this procedure can be applied to any map. The latter are used only to validate the result of the clustering in order to extract some information about the observed phenomena. To reduce the number of integrals to be solved and thus the calculation time, the pulses saturating the instrumentation, and which were identified as originating from the pulse generator of the PEA measurement, were previously eliminated. The remaining dataset has been provided as input to the clustering algorithm. Fig. 15 shows the waveforms and frequency spectra of the three main clusters identified. The largest of the three clusters (blue one) contains 3397 pulses with a shape and spectrum characteristic of a corona phenomenon [41]. The source of this type of discharge may be somewhere in the measurement setup where a spike effect occurs. The third cluster (yellow one) is concentrated in the initial part of the measurement and contains 331 pulses. This phenomenon can be identified as discharges due to the initial voltage increase.

The second cluster identified (orange one) is the most interesting. It is characterised by a recurrence of 495 pulses with a shape and spectrum typical of internal discharges. They occur with an oscillating waveform with a prevailing frequency of 33 MHz. The amplitude of these discharges is quite variable in the first phase of measurement, while with the passage of time it concentrates around a value of −50 mV.

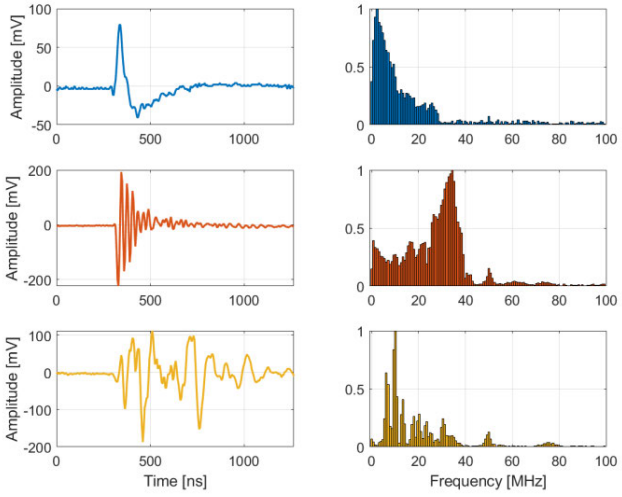

FIGURE 15. Detected pulses (on the left) and the related frequency spectrum (on the right) of the three different cluster. Based on pulse shape and frequency content, the blue pulses are associated to corona PD, the red one are attributed to internal PD, while the yellow one are due to generator voltage increasing.

Following the application of the clustering algorithm and the analysis based on cross-correlation, it is known how to separate the discharges. Fig. 16 and Fig. 17 show the various points of the TRPD pattern and of the TF map coloured and marked according to the cluster they belong to. For the sake of easy reading of the image, only the main clusters are shown, i.e. those with a number greater than 300 pulses. From Fig. 16, it shows the presence of one type of pulses occurred at the beginning of the test, another type of pulses is characterized by positive sign and variable amplitude, while the third one is negative and more concentrated in amplitude. From Fig. 17, it can be seen that the two patterns shown in blue and yellow overlap. Replicating this result with traditional clustering algorithms would have been a challenge. The difference among the orange clustered pulses with the other two depicted in blue and yellow results more evident.

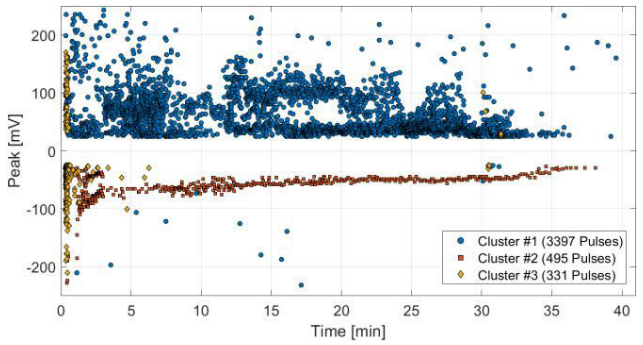

FIGURE 16. The related clustered TRPD pattern. It shows the presence of one type of pulses occurred at the beginning of the test, another type of pulses is characterized by positive sign and variable amplitude, while the third one is negative and more concentrated in amplitude.

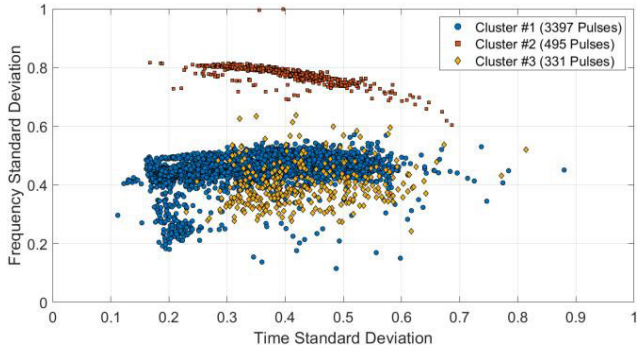

FIGURE 17. The related clustered TF Map. The difference among the red clustered pulses with the other two depicted in blue and yellow results more evident.

VII. DISCUSSION

The interaction between the electric field radial distribution changing over time and the PD inception and evolution have been investigated. The signal coming from both PEA cell and PD measurement system have been acquired simultaneously in two different portions of the same cable as depicted in Fig. 18. For issues linked to the dielectric acoustic transfer function update during thermal transients, the cable was preliminarily subjected to a thermal gradient waiting a steady state condition with a $\Delta T = 11\ ^{\circ}C$ between the core and the external outer interface [42]. In this way, the PEA signal processing is equal for all the acquired profiles. In the previous paper [22], with the same purpose to link the electric field changes to PD phenomena, the current load and voltage were applied at the same time. In that work, only PDs were detected experimentally and their triggering was correlated with the PDIEF by means of electric field simulations performed with Comsol Multiphysics. In the present work, the voltage was applied after that the thermal steady state was reached. Therefore, the acquisition of space charge profiles from the PEA cell was performed only during the electrical transient. In this way, it was possible to acquire and compare the evolution of the electric field with the PD phenomenon over time.

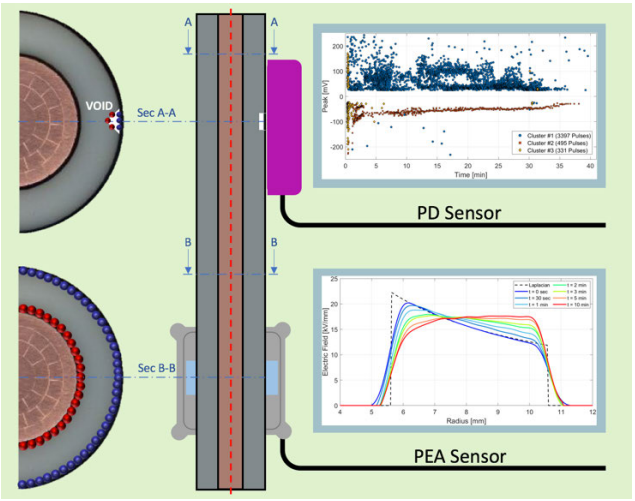

FIGURE 18. Simultaneous measurements of PD and PEA signals in two different section of the cable.

As described in the Section V, a very fast electric field transient has been observed. Choosing as a reference radial position that one in correspondence of the dielectric/outer semicon interface, in Fig. 11 it can be observed that the electric field varies very quickly, reaching the steady state condition after just 10 minutes. In particular, the 60% increase of the electric field was concentrated in the first 2 minutes, with the electric field that varying from 12 kV/mm to 15 kV/mm, reaching the 98% of the final steady state value of 17 kV/mm after 5 minutes.

At the same time, in Section VI, after the clustering process, the TRPD trend over time of the discharges generated in a cavity located in the same radial position have been acquired and have been shown in Fig. 16. In this trend we can observe the triggering of the discharges, the evolution over time and the final extinction of the phenomenon. Fig. 19 shows a direct comparison of the outer electric field evolution over time and the activity of internal discharges only. It can be observed that the PD are triggered after 1 minute, corresponding to a PDIEF of 12.6 kV/mm. This result agrees with what was obtained in the previous experiment described in [22]. In fact, an electric field value of 12.6 kV/mm in the healthy dielectric section corresponds to an electric field of approximately 17.95 kV/mm, obtained from the simulated trend in Fig. 12.

After the triggering, PDs with higher amplitude were observed until the electric field reached the steady state condition. Subsequently, the amplitude of the discharges is more stable and the value is around 50 mV.

The electric field value not only determines the PD onset but it is also directly linked to the PD Repetition Rate (PDRR) and PD magnitude.

In particular, under DC stress, the PD activity also depends on the time derivative of electric field *dE/dt* and on the time constant τ for charging the cavity. In the test described in this work, during the first 10 minutes of voltage application, the increasing trend of the field over time generates a high

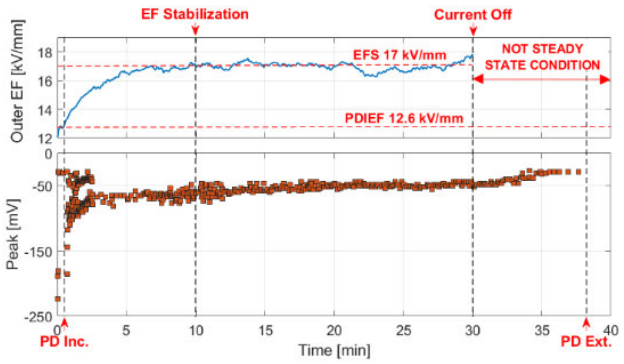

FIGURE 19. Electric field calculated in the healthy cable section and PD activity detected within the air void defect.

dE/dt. On the other hand, due to the presence of stationary thermal gradient, the τ parameter results constant. Therefore, during this first time interval, both parameters have a role in the PD activity, producing high PD magnitude and high PDRR. On the contrary, after few minutes of the electric field stabilization (which occurs at around 10 minutes), the *dE/dt* can be considered approximately equal to zero. Based on this, starting from electric field stabilization, only the τ (which under thermal steady state provides a constant PDRR) influences the discharge activity and therefore the PD magnitude and the PDRR decrease to a constant value with respect to their values observed at the beginning of the test.

In Fig. 20 it can be observed that after about 15 minutes, where the electric field was in steady state condition, the PDRR results almost constant and around 10 discharges per minute. After 30 minutes, the current load was switched off and the PDRR decreased until extinction at 38 minutes. In this time interval, such as from 30 to 40 minutes, it was not possible to acquire the corresponding electric field value. This is because switching off the current in the cable triggers a thermal transient which no longer allows the correct processing of the charge profiles acquired with the PEA cell.

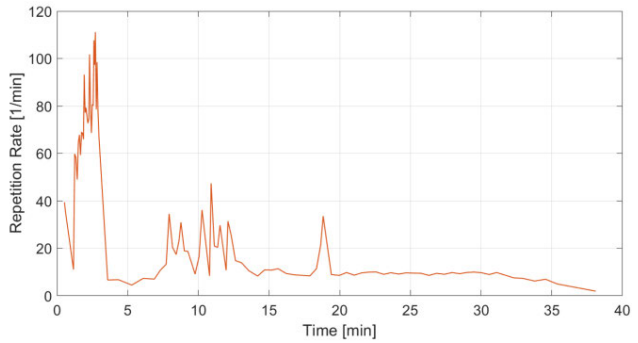

FIGURE 20. Partial discharge repetition rate over time.

The obtained numerical results concerning the accumulated charge density and the related electric field calculated in the outer radius of the healthy cable section, the PDRR values and the maximum PD amplitude are summarized in Table 3.

TABLE 3. Summarized experimental results related to the outer radius of the healthy cable section.

Time [min]	Space Charge [C/m^3]	Electric Field [kV/mm]	PDRR [1/min]	Maximum PD Amplitude [mV]
0	-0.38	12	/	/
0.5	-0.43	12.9	40	/
1	-0.46	13.9	20	109
2	-0.50	15	73	86
3	-0.53	15.5	71	67
5	-0.55	16.5	5.5	71
10	-0.57	17	17.5	61
20	-0.57	17	9	48
30	-0.66	17.8	9.5	48

VIII. CONCLUSION

This paper deals the correlation between the variable electric field distribution and the onset and evolution of PD in an HVDC cable under normal operating conditions. Experimental results showed that, based on the defect radial position, trigger of PD is strictly related to the electric field inversion phenomenon that, under DC stress, occurs only with the presence of a thermal gradient.

It was found that, after reaching thermal steady state gradient, the Laplacian electric field distribution observed at the beginning of the voltage application in positive polarity, changes very fast within few minutes. Therefore, at the beginning of the test, the maximum electric field value was observed in the internal cable insulating layer, while after 5 minutes, the maximum field occurred in the opposite insulating interface. The monitoring of PDs highlighted that their trigger occurs after 1 minute of voltage application and thus at the time instant in which the growing electric field, in the external cable insulating layer (in the radius where the air void defect is located), reaches the PDIEF of 12.6 kV/mm.

The electric field not only determined the PD onset but also, when reached the steady state conditions, produced a "*constant*" PDRR of 10 PD/min which is equivalent to one discharge every six seconds.

In conclusion, the scientific contributions of this research activity are listed below:

- a measurement setup for the simultaneous detection of space charge/electric field and PDs was proposed;
- a new PEA cell was developed and an in deep analysis of the acoustic wave behavior within its structure was addressed;
- the performance of the developed clustering algorithm for the PD signals separation under DC stress were confirmed.

Whereas, the main scientific results obtained in this work can be summarized as follow:

- after the thermal gradient was reached, the electric field transient results very fast as soon as the DC voltage is applied;
- in presence of a defect within the dielectric, the electric field radial distribution variations over time, until the inversion, strongly influence the PD triggering and RR;
- PDs end 8 minutes after removing the load current.

These results provide new knowledge on the interaction between electric field and PDs with a view to providing a contribution to the research for new HVDC systems reliability assessing techniques.

REFERENCES

[1] W. Wang, X. Yan, S. Li, L. Zhang, J. Ouyang, and X. Ni, "Failure of submarine cables used in high-voltage power transmission: Characteristics, mechanisms, key issues and prospects," *IET Gener., Transmiss. Distrib.*, vol. 15, no. 9, pp. 1387–1402, May 2021, doi: 10.1049/gtd2.12117.

[2] H. Yahyaoui, J. Castellon, S. Agnel, A. Hascoat, W. Frelin, C. Moreau, P. Hondaa, D. L. Roux, V. Eriksson, and C. J. Andersson, "Behavior of XLPE for HVDC cables under thermo-electrical stress: Experimental study and ageing kinetics proposal," *Energies*, vol. 14, no. 21, p. 7344, Nov. 2021, doi: 10.3390/en14217344.

[3] N. Rosle, N. A. Muhamad, M. N. K. H. Rohani, and M. K. M. Jamil, "Partial discharges classification methods in XLPE cable: A review," *IEEE Access*, vol. 9, pp. 133258–133273, 2021, doi: 10.1109/ACCESS.2021.3115519.

[4] X. Zhang, B. Pang, Y. Liu, S. Liu, P. Xu, Y. Li, Y. Liu, L. Qi, and Q. Xie, "Review on detection and analysis of partial discharge along power cables," *Energies*, vol. 14, no. 22, p. 7692, Nov. 2021, doi: 10.3390/en14227692.

[5] G. V. R. Xavier, H. S. Silva, E. G. da Costa, A. J. R. Serres, N. B. Carvalho, and A. S. R. Oliveira, "Detection, classification and location of sources of partial discharges using the radiometric method: Trends, challenges and open issues," *IEEE Access*, vol. 9, pp. 110787–110810, 2021, doi: 10.1109/ACCESS.2021.3102888.

[6] P. H. F. Morshuis and J. J. Smit, "Partial discharges at DC voltage: Their mechanism, detection and analysis," *IEEE Trans. Dielectr. Electr. Insul.*, vol. 12, no. 2, pp. 328–340, Apr. 2005.

[7] P. Romano, A. Imburgia, G. Rizzo, G. Ala, and R. Candela, "A new approach to partial discharge detection under DC voltage: Application to different materials," *IEEE Elect. Insul. Mag.*, vol. 37, no. 2, pp. 18–32, Mar. 2021, doi: 10.1109/MEI.2021.9352713.

[8] G. Mazzanti and M. Marzinotto, *Extruded Cables for High-Voltage Direct-Current Transmission: Advances in Research and Development* (Power Engineering Series). Hoboken, NJ, USA: Wiley, 2013.

[9] Y. Zhou, S. Peng, J. Hu, and J. He, "Polymeric insulation materials for HVDC cables: Development, challenges and future perspective," *IEEE Trans. Dielectr. Electr. Insul.*, vol. 24, no. 3, pp. 1308–1318, Jun. 2017, doi: 10.1109/TDEI.2017.006205.

[10] M. J. P. Jeroense and P. H. F. Morshuis, "Electric fields in HVDC paper-insulated cables," *IEEE Trans. Dielectr. Electr. Insul.*, vol. 5, no. 2, pp. 225–236, Apr. 1998, doi: 10.1109/94.671940.

[11] S. Kumara, Y. V. Serdyuk, and M. Jeroense, "Calculation of electric fields in HVDC cables: Comparison of different models," *IEEE Trans. Dielectr. Electr. Insul.*, vol. 28, no. 3, pp. 1070–1078, Jun. 2021, doi: 10.1109/TDEI.2021.009371.

[12] G. Teyssedre, T. T. N. Vu, and S. L. Roy, "Insulating materials for HVDC cable accessories: Effects on the electric field in nonstationary situations," *IEEE Elect. Insul. Mag.*, vol. 38, no. 5, pp. 6–17, Sep. 2022, doi: 10.1109/MEI.2022.9858038.

[13] Y. Zhan, G. Chen, M. Hao, L. Pu, X. Zhao, H. Sun, S. Wang, A. Guo, and J. Liu, "Comparison of two models on simulating electric field in HVDC cable insulation," *IEEE Trans. Dielectr. Electr. Insul.*, vol. 26, no. 4, pp. 1107–1115, Aug. 2019, doi: 10.1109/TDEI.2019.007878.

[14] H. Ren, L. Zhong, X. Yang, W. Li, J. Gao, Q. Yu, X. Chen, and Z. Li, "Electric field distribution based on radial nonuniform conductivity in HVDC XLPE cable insulation," *IEEE Trans. Dielectr. Electr. Insul.*, vol. 27, no. 1, pp. 121–127, Feb. 2020, doi: 10.1109/TDEI.2019.008345.

[15] F. Mauseth and H. Haugdal, "Electric field simulations of high voltage DC extruded cable systems," *IEEE Elect. Insul. Mag.*, vol. 33, no. 4, pp. 16–21, Jul. 2017, doi: 10.1109/MEI.2017.7956628.

[16] L. Chen, X. Gu, and Y. Xu, "Modelling of enhancement of electric field and temperature on partial discharge in the XLPE cavity model under positive DC voltage," in *Proc. Asia Energy Electr. Eng. Symp. (AEEES)*, Chengdu, China, May 2020, pp. 454–458, doi: 10.1109/AEEES48850.2020.9121565.

[17] Y. Zhu, F. Yang, X. Xie, W. Cao, G. Sheng, and X. Jiang, "Studies on electric field distribution and partial discharges of XLPE cable at DC voltage," in *Proc. 12th Int. Conf. Properties Appl. Dielectric Mater. (ICPADM)*, China, May 2018, pp. 562–565, doi: 10.1109/ICPADM.2018.8401106.

[18] A. Sahu, R. Sahoo, and S. Karmakar, "The study of electric field and partial discharges on XLPE insulation under DC high voltage using COMSOL multiphysics," in *Proc. 3rd Int. Conf. High Voltage Eng. Power Syst. (ICHVEPS)*, Bandung, Indonesia, Oct. 2021, pp. 309–313, doi: 10.1109/ICHVEPS53178.2021.9600924.

[19] P. Seri, G. C. Montanari, M. Albertini, and S. Franchi Bononi, "Electrothermal aging of DC cables and insulation electrical properties: Conductivity, space charge and partial discharges," in *Proc. IEEE Electr. Insul. Conf. (EIC)*, Knoxville, TN, USA, Jun. 2022, pp. 13–16, doi: 10.1109/EIC51169.2022.9833209.

[20] A. Cavallini, F. Ciani, and G. C. Montanari, "The effect of space charge on phenomenology of partial discharges in insulation cavities," in *Proc. Annu. Rep. Conf. Elect. Insul. Dielectric Phenomena*, Nashville, TN, USA, Oct. 2005, pp. 410–413, doi: 10.1109/CEIDP.2005.1560707.

[21] H. Naderiallaf, P. Seri, and G. C. Montanari, "Designing a HVDC insulation system to endure electrical and thermal stresses under operation. Part I: Partial discharge magnitude and repetition rate during transients and in DC steady state," *IEEE Access*, vol. 9, pp. 35730–35739, 2021, doi: 10.1109/ACCESS.2021.3062440.

[22] G. Rizzo, P. Romano, A. Imburgia, and G. Ala, "Partial discharges in HVDC cables—The effect of the temperature gradient during load transients," *IEEE Trans. Dielectr. Electr. Insul.*, vol. 28, no. 5, pp. 1767–1774, Oct. 2021, doi: 10.1109/TDEI.2021.009602.

[23] A. Imburgia, A. D. Fatta, P. Romano, G. Rizzo, V. L. Vigni, and G. Ala, "A study on partial discharges pattern recognition under DC voltage through clustering algorithms and cross correlation filter," *IEEE Trans. Dielectr. Electr. Insul.*, vol. 30, no. 6, pp. 2543–2550, Dec. 2023, doi: 10.1109/TDEI.2023.3308532.

[24] G. Ala, M. Caruso, V. Cecconi, S. Ganci, A. Imburgia, R. Miceli, P. Romano, and F. Viola, "Review of acoustic methods for space charge measurement," in *Proc. AEIT Int. Annu. Conf. (AEIT)*, Naples, Italy, Oct. 2015, pp. 1–6, doi: 10.1109/AEIT.2015.7415270.

[25] S. Zahra, S. Morita, M. Utagawa, T. Kawashima, Y. Murakami, N. Hozumi, P. Morshuis, Y.-I. Cho, and Y.-H. Kim, "Space charge measurement equipment for full-scale HVDC cables using electrically insulating polymeric acoustic coupler," *IEEE Trans. Dielectr. Electr. Insul.*, vol. 29, no. 3, pp. 1053–1061, Jun. 2022, doi: 10.1109/TDEI.2022.3169106.

[26] A. Imburgia, P. Romano, G. Chen, G. Rizzo, E. Riva Sanseverino, F. Viola, and G. Ala, "The industrial applicability of PEA space charge measurements, for performance optimization of HVDC power cables," *Energies*, vol. 12, no. 21, p. 4186, Nov. 2019, doi: 10.3390/en12214186.

[27] K. Wu, R. Su, and X. Wang, "Space charge behavior in polymeric materials under temperature gradient," *IEEE Elect. Insul. Mag.*, vol. 36, no. 2, pp. 37–49, Mar. 2020, doi: 10.1109/MEI.2020.9070115.

[28] R. Bodega, P. H. F. Morshuis, and J. J. Smit, "Space charge measurements on multi-dielectrics by means of the pulsed electroacoustic method," *IEEE Trans. Dielectr. Electr. Insul.*, vol. 13, no. 2, pp. 272–281, Apr. 2006.

[29] A. Imburgia, P. Romano, E. R. Sanseverino, L. De Rai, S. F. Bononi, and I. troia, "Pulsed electro-acoustic method for specimens and cables employed in HVDC systems: Some feasibility considerations," in *Proc. AEIT Int. Annu. Conf.*, Bari, Italy, Oct. 2018, pp. 1–6, doi: 10.23919/AEIT.2018.8577421.

[30] Y. Li, M. Yasuda, and T. Takada, "Pulsed electroacoustic method for measurement of charge accumulation in solid dielectrics," *IEEE Trans. Dielectr. Electr. Insul.*, vol. 1, no. 2, pp. 188–195, Apr. 1994, doi: 10.1109/94.300251.

[31] A. Imburgia, P. Romano, G. Rizzo, F. Viola, G. Ala, and G. Chen, "Reliability of PEA measurement in presence of an air void defect," *Energies*, vol. 13, no. 21, p. 5652, Oct. 2020, doi: 10.3390/en13215652.

[32] M. Fu and G. Chen, "Space charge measurement in polymer insulated power cables using flat ground electrode PEA system," *IEE Proc.-Sci., Meas. Technol.*, vol. 150, no. 2, pp. 89–96, 2003.

[33] N. Hozumi, "Space charge measurement techniques for practical insulation systems," in *Proc. IEEE 4th Int. Conf. Elect. Mater. Power Equip. (ICEMPE)*, Shanghai, China, May 2023, pp. 1–8, doi: 10.1109/ICEMPE57831.2023.10139742.

[34] N. Hozumi, E. B. Prastika, S. Zahra, T. Kawashima, and Y. Murakami, "Dual-domain deconvolution process applied to time-resolved quantitative dielectric measurement," in *Proc. IEEE 3rd Int. Conf. Dielectr. (ICD)*, Jul. 2020, pp. 347–350.

[35] E. B. Prastika, S. Zahra, X. Li, Y. Murakami, T. Kawashima, N. Hozumi, and Y. Kim, "The application of signal processing using dual domain deconvolution for new space charge measurement method in HVDC full-size cables," in *Proc. Int. Symp. Electr. Insulating Mater. (ISEIM)*, Sep. 2020, pp. 277–280.
[36] A. Yeongguk, X. Li, T. Kawashima, Y. Murakami, and N. Hozumi, "Signal processing for space charge measurement using Laplace deconvolution," in *Proc. 9th Int. Conf. Condition Monitor. Diagnosis (CMD)*, Nov. 2022, pp. 811–814.
[37] M. Fu, G. Chen, A. E. Davies, and J. G. Head, "Space charge measurements in power cables using a modified PEA system," in *Proc. 8th Int. Conf. Dielectric Mater., Meas. Appl.*, Edinburgh, U.K., 2000, pp. 74–79, doi: 10.1049/cp:20000480.
[38] H. Illias, T. Soon Yuan, A. H. A. Bakar, H. Mokhlis, G. Chen, and P. L. Lewin, "Partial discharge patterns in high voltage insulation," in *Proc. IEEE Int. Conf. Power Energy (PECon)*, Kota Kinabalu, Malaysia, Dec. 2012, pp. 750–755, doi: 10.1109/PECON.2012.6450316.
[39] A. Di Fatta, A. Imburgia, G. Rizzo, G. Akbar, V. L. Vigni, P. Romano, and G. Ala, "Partial discharge separation by using pulses cross-correlation," in *Proc. IEEE Conf. Elect. Insul. Dielectric Phenomena (CEIDP)*, East Rutherford, NJ, USA, Oct. 2023, pp. 1–4, doi: 10.1109/CEIDP51414.2023.10410547.
[40] A. Di Fatta, A. Imburgia, G. Rizzo, G. Akbar, V. L. Vigni, P. Romano, and G. Ala, "Modified hierarchical clustering algorithm for partial discharge separation," in *Proc. IEEE Conf. Elect. Insul. Dielectric Phenomena (CEIDP)*, East Rutherford, NJ, USA, Oct. 2023, pp. 1–4, doi: 10.1109/CEIDP51414.2023.10410179.
[41] P. Romano, A. Imburgia, and G. Ala, "Partial discharge detection using a spherical electromagnetic sensor," *Sensors*, vol. 19, no. 5, p. 1014, Feb. 2019, doi: 10.3390/s19051014.
[42] H. Wang, K. Wu, Q. Zhu, and X. Wang, "Recovery algorithm for space charge waveform under temperature gradient in PEA method," *IEEE Trans. Dielectr. Electr. Insul.*, vol. 22, no. 2, pp. 1213–1219, Apr. 2015, doi: 10.1109/TDEI.2015.7076824.

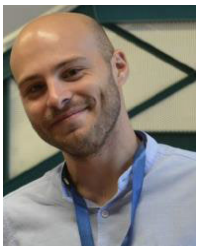

ALESSIO DI FATTA (Member, IEEE) received the master's degree in electrical engineering from the University of Palermo, Palermo, Italy, in 2022, where he is currently pursuing the Ph.D. degree with the Department of Engineering. His research interests include HVDC systems, partial discharge measurement and pattern recognition algorithms, space charge accumulation, and insulating systems diagnosis.

PIETRO ROMANO (Senior Member, IEEE) received the M.Sc. and Ph.D. degrees in electrical engineering from the University of Palermo, Palermo, Italy, in 1993 and 1998, respectively. He is currently an Associate Professor with the Department of Engineering, University of Palermo, and teaches basic electrical engineering, electrotechnics, and insulation systems diagnostics. He is the Head of the L.E.PR.E. HV Laboratory, University of Palermo. His research activity is mainly in the fields of insulating systems diagnosis, partial discharge and space charge measurements, HV systems, HVDC cable systems, multifactor stress effects, and electric field simulations. He is a member of Italian AG of European SET Plan WG HVDC, the IEEE DEIS Meetings Committee, the IEEE DEIS CEIDP Board, the IEEE DEIS ICD Committee, and CIGRE AG D1.03 "Solid materials."

GIUSEPPE RIZZO (Member, IEEE) was born in 1984. He received the master's degree in nuclear engineering and the Ph.D. degree defending a thesis focused on the role of space charge phenomena in HVDC applications from the University of Palermo, Palermo, Italy, in 2008 and 2021, respectively. From 2009 to 2018, he was a Researcher and Designer of small wind turbine generators (SWTG) with Jonica Impianti. Since 2021, he has been employed in EOSS (Prysmian Group) as Research and Development Software Engineer and his activity is focused on the development of real time thermal rating algorithms.

GUIDO ALA (Senior Member, IEEE) has been the Director of the Laboratory for Modeling and Electromagnetic Simulation (MOSEM-Lab), Since 2012. He is currently a Full Professor of electrical engineering—SC 09/E1 from "Dipartimento di Ingegneria," University of Palermo, Palermo, Italy. His main research interests include computational electromagnetics (including MoM, FDTD, application of wavelets, and mesh-free innovative numerical approach), electromagnetic transient analysis, lightning, electromagnetic compatibility, optimized design of EMI filters and power electronics converters, partial discharge detection, biomedical engineering (including magnetoencephalography and electroencephalography innovative numerical modelling, and electromagnetic fields effect on humans), electrical systems design for fusion engineering, innovative solutions for sustainable mobility (including photovoltaic applications) in the smart cities context, and electrical analogies in material's viscoelasticity behavior.

ANTONINO IMBURGIA (Member, IEEE) received the M.Sc. and Ph.D. degrees in electrical engineering from the University of Palermo, Palermo, Italy, in 2014 and 2018, respectively. Since 2015, he collaborates in the research activities with the L.E.PR.E. HV Laboratory, University of Palermo. He is currently a Researcher with the Department of Engineering, University of Palermo. His research interests include HVDC, space charge distribution in solid dielectrics and its detection by means of the PEA method, insulating systems diagnosis, and partial discharge measurements under ac and dc stresses.

Open Access funding provided by 'Università degli Studi di Palermo' within the CRUI CARE Agreement